The Thesis Committee for Rithvik Ramesh
Certifies that this is the approved version of the following Thesis:

Engineering of the Interband Second Order Optical Nonlinearity Using Asymmetric Coupled Quantum Wells

APPROVED BY
SUPERVISING COMMITTEE:

Seth R. Bank, Supervisor

Daniel Wasserman

Engineering of the Interband Second Order Optical Nonlinearity Using Asymmetric Coupled Quantum Wells

by

Rithvik Ramesh

Thesis

Presented to the Faculty of the Graduate School of

The University of Texas at Austin

in Partial Fulfillment

of the Requirements

for the Degree of

Master of Science in Engineering

The University of Texas at Austin

May 2023

Abstract

Engineering of the Interband Second Order Optical Nonlinearity Using Asymmetric Coupled Quantum Wells

Rithvik Ramesh, MSE

The University of Texas at Austin, 2023

Supervisor: Seth R. Bank

Developing a semiconductor platform with strong second-order optical nonlinearity can enable better integration with semiconductor photonics and improved performance compared to traditional nonlinear optical materials (i.e. $LiNbO_3$). In a coupled quantum well structure, the quantum well thicknesses, tunneling barrier thickness, material compositions, and other parameters can be designed to tune the second-order susceptibility, $\chi^{(2)}$. Utilizing interband transitions allows access to energy level transitions across the bandgap, thus enabling strong, tunable $\chi^{(2)}$ in the near-IR. Schrodinger-Poisson methods and density functional theory were used to calculate the second-harmonic generation $\chi^{(2)}$ for GaAs/AlGaAs coupled quantum well structures. By using rigorous wavefunction calculation methods and considering all possible transitions contributing to second-harmonic generation, multiple methods to enhance and tailor $\chi^{(2)}$ have been determined. Using coupled asymmetric GaAs/AlGaAs quantum wells and varying the quantum well thicknesses, the 50 meV off-resonant wavelength for $\chi^{(2)}$ can be tuned across the optical communications wavelengths between 1.5 m and 1.7 m. This

work lays the foundation for designing III-V superlattices and digital alloys with enhanced second-order optical nonlinearities that can be tailored for the wavelength requirements of particular applications.

Portions of this Thesis, including the abstract, are part of a publication in preparation.

Table of Contents

List of Figures

Chapter 1: Introduction and Background

MOTIVATION

Nonlinear optical processes are becoming increasingly important for applications in optical communications, information processing, quantum photonics, spectroscopy, integrated photonics, optical frequency combs, and high energy lasers [1][2][3][4][5][6]. Second-order optical nonlinearities are particularly practical because they require significantly lower light intensities than third-order nonlinearities. The second-order family of nonlinear optical processes includes second harmonic generation, sum and difference frequency generation, and the electro-optic effect [7]. The electro-optic Pockel's effect in particular has found widespread applications in optical modulators [8]. By applying a voltage across the nonlinear material, the electric field induces a change in the refractive index. This can be used to change the effective path length of light travelling through the material, which is the working principle for Mach-Zender interferometer modulators [8]. Electro-optic modulators are already used widely for optical interconnects in data centers, where the low latency and high bandwidth offered by photonics is an especially important advantage over electronics [9]. With the development of integrated photonics, the use of electro-optic modulators and other nonlinear optical devices will proliferate [10].

Second order optical nonlinearity also has important roles in laser design and experimental physics. Second harmonic generation is often used to double the frequency of light, and optical parametric amplification is a three-wave mixing process to amplify a signal at a particular wavelength using a pump at a more easily generated wavelength [11][7]. Short pulse, ultra-high energy lasers, such as the Texas Petawatt laser, also utilize optical parametric amplification to amplify chirped pulse signals [12].

However, second-order nonlinearity requires non-centrosymmetric materials [13]. Traditional second-order nonlinear optical materials, such as lithium niobate, have inherently strong second order susceptibility, $\chi^{(2)}$, and can be grown reliably with high quality [14]. While such complex oxides can have strong nonlinearities, they are generally difficult to integrate with semiconductor substrates, making it difficult to use the complex oxides with silicon photonics or semiconductor photonics platforms [15]. Furthermore, devices using traditional nonlinear materials need to be large to increase the interaction length or rely on electric field concentration to overcome the inherent weakness of nonlinear optical processes [14].

As a result, there is significant interest in developing a semiconductor material platform with large and tunable second order nonlinearity. The semiconductor digital alloy platform is well suited for tunable nonlinearities because the band offsets, band gaps, and layer thicknesses of the semiconductor heterostructure can be very finely controlled [16]. Intersubband optical nonlinearities in semiconductor structures have been shown to be very strong (on the order of 10 nm/V) for input wavelengths in the mid to far infrared [17]. However, it is important to achieve strong and tunable nonlinearities in the near-IR, specifically the optical communication S, C, L, and U bands from 1450 - 1700 nm. Thus, the goal is to design semiconductor structures with interband optical nonlinearities, such that transitions across the bandgap enable $\chi^{(2)}$ at higher energies.

SECOND-ORDER NONLINEAR OPTICAL SUSCEPTIBILITY

Under strong electric field, higher order terms of the material polarization become important. The strength of each term in the expansion of polarization is characterized by a susceptibility, $\chi^{(n)}$. Using the density matrix formalism, the second order susceptibility for a multi-quantum well structure is given by equation 1 [18].

$$\chi_{ijk}^{(2)}(\omega_1,\omega_2)=\frac{N_z e^3}{2\epsilon_0\hbar^2}\sum_P\sum_{b_1,b_2,b_3}\sum_{l,m,n}f_{b,l}\sum_{k_{||}}\frac{\langle\phi_{1,l}^*|r_i|\phi_{2,m}\rangle\langle\phi_{2,m}^*|r_j|\phi_{3,n}\rangle\langle\phi_{3,n}^*|r_k|\phi_{1,l}\rangle}{[\omega_{b_2,m}(k_{||})-\omega_{b_1,l}(k_{||})-\omega_1-\omega_2][\omega_{b_3,n}(k_{||})-\omega_{b_1,l}(k_{||})-\omega_2]} \quad (1)$$

For interband nonlinearity operating near resonance, the transitions will occur between the bound states in the conduction band and valence band that are closest to the band edge. Since heavy hole states lie higher in energy than light hole states, the relevant transitions will occur between heavy hole and electron states [19]. Because this is an interband process, the ground states of the transitions are filled valence states, so the fermi function of the ground state, $f_{b,l}$, is 1. The light propagates in the xy plane (growth direction is z) such that the electric field portion of the EM radiation is along the growth direction [20]. It is necessary for the electric field to be perpendicular to the plane of the quantum wells to generate nonlinear polarization of the quantum well states. As a result, only the $\chi_{xzx}^{(2)}$ tensor element is nonvanishing [20]. Averaging over the polarization directions reduces the sum over the polarizations and introduces a factor of 1/3.

The wavefunctions in the matrix elements can be split into the envelope and unit cell portions. This is used to simplify the interband and intersubband matrix elements. In the intersubband case, only the matrix element with respect to the growth direction is nonvanishing, so without loss of generality the r_i factor can be replaced with z. Because both wavefunctions belong to the same band, the unit cell portions of the wavefunctions are the same, so the matrix element of the unit cell portions is equal to 1. For the interband matrix element, the interband matrix element of the unit cell portions of the wavefunctions can be factored out. What remains is the inner product of the envelope wavefunctions in the conduction band and valence band. Because the interband matrix element of the Bloch unit cell wavefunctions is constant regardless of which heavy hole and electron states are considered, it can be factored out of the summation. It is also not a function of the wavevector, so it can be treated as a constant. Because each term has two

interband matrix elements, the interband matrix element of the unit cell wavefunctions, $r_{e,hh}$, is squared and included with the prefactors of the equation. Equations 2 and 3 show how the matrix elements are treated mathematically.

$$\langle \phi^*_{b,m} | r_i | \phi_{b,n} \rangle = \langle \psi_{b,m} | z | \psi_{b,n} \rangle \delta_{i,z} \quad (2)$$

$$\langle \phi^*_{e,m} | r_i | \phi_{hh,n} \rangle = \langle \psi_{e,m} | \psi_{hh,n} \rangle r_{e,hh} \quad (3)$$

With these assumptions and separating the envelope and unit cell portions of the wavefunctions, the equation for $\chi^{(2)}$ simplifies to equation 4 [20].

$$\chi^{(2)}_{xzx}(\omega_1, \omega_2) = \frac{N_z e^3 r^2_{e,hh}}{6\epsilon_0 \hbar^2} \sum_{k_{||}} \sum_{m.n} \left(\sum_{l} \frac{(\psi_{hhm}|\psi_{en})\langle \psi_{en}|z|\psi_{el}\rangle(\psi_{el}|\psi_{hhm})}{[\omega^{en}_{hhm}(k_{||}) - \omega_1 - \omega_2][\omega^{el}_{hhm}(k_{||}) - \omega_1]]} \right.$$
$$\left. - \frac{(\psi_{en}|\psi_{hhm})\langle \psi_{hhm}|z|\psi_{hhl}\rangle(\psi_{hhl}|\psi_{en})}{[\omega^{en}_{hhm}(k_{||}) - \omega_1 - \omega_2][\omega^{en}_{hhl}(k_{||}) - \omega_1]]} \right) \quad (4)$$

In equation 4, $r_{e,hh}$ is the interband matrix element of the Bloch unit cell wavefunctions in the conduction and valence bands, N_z is the number of quantum wells per unit length, ω_1 and ω_2 are the input photon frequencies, ω^{en}_{hhm} is the frequency of the transition between the denoted energy levels at the given wavevector $k_{||}$, and [m,n,l] are used to index the energy levels such that the summation over [m,n,l] considers all possible transitions between the first two heavy hole and electron states. The first term within the summation is called the electron susceptibility and the second, negative term is called the hole susceptibility as they contain the intersubband matrix elements of the electrons and holes, respectively [20].

Understanding the units provides further insight to the $\chi^{(2)}$ equation. For the electron and hole susceptibility terms, the numerators have one dimension of length from the intersubband matrix element. In the cases when the indices $n = l$ or $m = l$, the two wavefunctions in the intersubband matrix element are the same. As a result, the term is essentially calculating the expectation value of the position of the charge relative to the

center of the entire quantum well region. This corresponds to a dipole (displaced charge) and the DC optical rectification process related to $\chi^{(2)}$. The interband inner products are unitless, but the interband matrix elements of the Bloch wavefunctions each carry one dimension of length. The denominator of each term has units of angular frequency squared. When considered in combination with $\frac{1}{\hbar^2}$ prefactor, there are units of energy in the denominator. Lastly, N_z is defined as the number of quantum wells per unit length. Overall, the units of $\chi^{(2)}$ are m/V, and typical order of magnitude for $\chi^{(2)}$ of bulk materials is 1 – 100 pm/V [21].

ASYMMETRIC COUPLED QUANTUM WELL STRUCTURE

The key terms in equation 2 are the interband and intersubband matrix elements in the numerator of each term and the transition energies in the denominators. The asymmetric coupled quantum well structure is used to introduce asymmetry at the structural level. Through bandgap engineering of the coupled quantum well structure, the electron and hole wavefunctions can be shaped to optimize the interband and intersubband matrix elements. The energy levels can also be tuned to enable strongest $\chi^{(2)}$ for input wavelengths of interest. Structure parameters to tune the dipole matrix elements and energy levels include the quantum well widths, coupling barrier thickness, conduction and valence band energy offsets, and bandgaps of the quantum well and barrier materials. Graded alloy compositions in the wells and applied electric fields can be used to further engineer the energy bands of the structure.

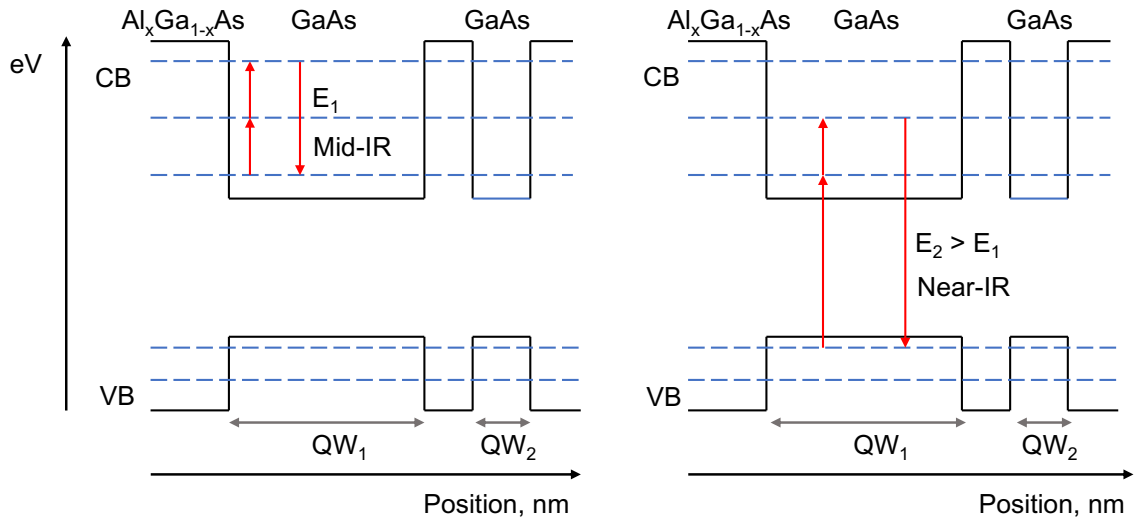

Figure 1: Asymmetric coupled quantum wells for intersubband and interband nonlinearities.

The diagram in figure 1 shows the asymmetric coupled quantum well structures with intersubband and interband sum-frequency generation processes illustrated by arrows between the energy levels. Utilizing interband transitions enables nonlinearity at higher energies than is achievable with intersubband approaches.

A pair of asymmetric coupled GaAs quantum wells (QW) in AlGaAs was used as a prototype material system and structure for $\chi^{(2)}$ calculations. The coupled quantum wells are symmetric when they have the same thickness and are asymmetric with asymmetry parameter s= $\frac{QW_1-QW_2}{QW_1+QW_2}$, where QW_1 and QW_2 are the thicknesses of quantum wells 1 and 2, respectively. By this definition, s=0 corresponds to a symmetric case, and in the limit of s=1, there is only one QW as the other has zero thickness. The GaAs/AlGaAs system was chosen as a prototype because the material and optical properties are well known, and because the precise growth of GaAs/AlGaAs structures is readily achievable using molecular beam epitaxy. This structure also consists of only one set of coupled quantum wells in order to best study the effect of varying each structure

parameter. The asymmetric coupled quantum well structure can be periodically repeated to enhance $\chi^{(2)}$ further and to ensure a sufficiently thick QW region for second-harmonic generation experiments [16]. In this work, the total QW thickness (QW_{tot}=QW_1+QW_2) varies between 5 nm and 12.5 nm, and the barrier thickness is 1 nm.

Chapter 2: $\chi^{(2)}$ Calculation Methods

WAVEFUNCTIONS AND ENERGY LEVELS

In order to calculate the $\chi^{(2)}$, the energy levels of the various electron and hole states and the transition dipole matric elements between them need to be determined. Only the heavy-hole states are considered in the valence band. For light-hole states, the effective mass is similar to that of electrons, so the light-hole and electron wavefunctions are similar, thus their intersubband matrix elements are similar and the terms cancel. Heavy-hole states are more confined in the QWs compared to electrons due to their larger effective mass, so the heavy-hole intersubband matrix element is in general smaller than that of the electrons. Thus, the negative term in the $\chi^{(2)}$ equation is small and does not cancel the positive term associated with electrons [19]. Furthermore, heavy-hole states lie closer to the valence band-edge than light-hole states, so heavy-hole states more strongly contribute to resonant or slightly-detuned $\chi^{(2)}$ processes near the band gap [19].

A Schrodinger-Poisson solver is used to determine the electron and heavy hole energy levels and associated envelope wavefunctions [22]. The interband and intersubband transition dipole matrix elements are calculated from the associated wavefunctions. The asymmetric coupled quantum well structure was defined layer-by-layer in the Nextnano Schrodinger-Poisson solver. Each layer is defined by the material, associated alloy compositions, thickness, doping type and level, and type of contact (if applicable. Within the Nextnano software, each material parameter was defined as a variable, and nested loops enabled calculating the wavefunctions and energy levels of each structure as certain parameters were swept. To efficiently sweep variables across wide ranges with high resolution, the simulation was optimized for short computation times. Specifically, the resolution of the calculation was reduced in the buffer regions.

Within the quantum well regions and coupling barrier layer, the quantum calculation is performed at every 0.01 nm, and in the buffer regions, the calculation is performed every 0.1 nm. Additionally, the simulation is run using single band solvers as opposed to the more rigorous 8-band k.p. model. This choice is justified because we are primarily concerned with energy bands and absorption/emission processes near zone-center ($k = 0$ $[m^{-1}]$). When considering nonlinear optical processes close to resonance with photon energies close to the band gap, processes occurring near zone-center will dominate. Strain is also negligible because the substrate material was defined in the software such that the quantum well and barrier layers are lattice-matched to the substrate. For the GaAs/AlGaAs coupled quantum wells, a GaAs substrate was used. In general, substrate material, layer thicknesses, doping concentrations, and other design parameters were chosen within the bounds of growth using molecular beam epitaxy (MBE). This was to ensure that designs proposed in simulation could be grown and characterized in experiment. Figure 2 shows the band-edge diagram of an asymmetric coupled quantum well structure with the first two electron and heavy hole energy levels and corresponding wavefunctions.

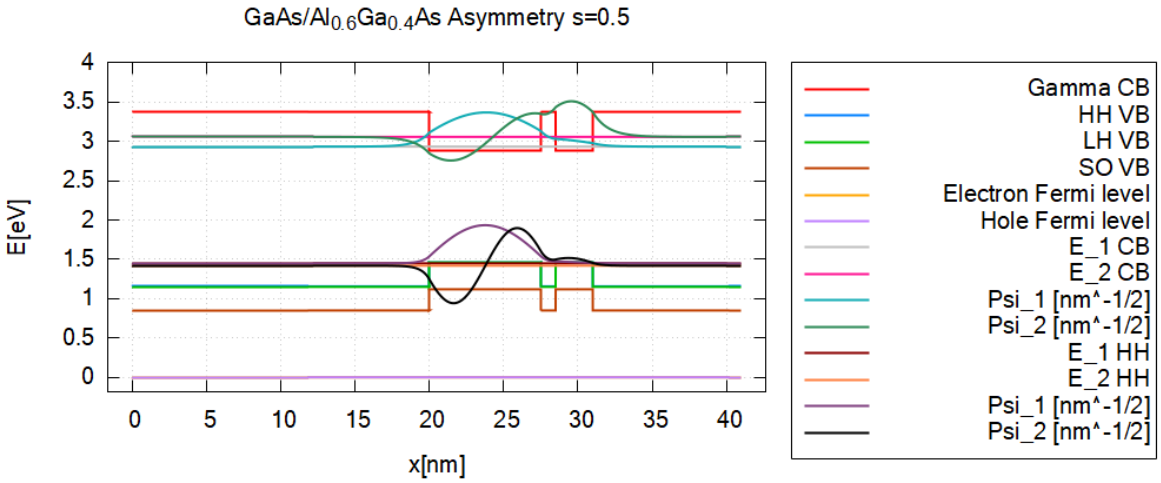

Figure 2: Band-edge diagram and wavefunctions

The interband matrix element of the unit cell wavefunctions was determined using density functional theory (DFT) using Vienna Ab initio Simulation Package (VASP) with HSE06 hybrid functionals. This work was performed by our collaborators at Texas State University. The value for the interband matrix element of the Bloch wavefunctions for GaAs was found to be $r_{e,hh} \cong 0.6$ Å.

$\chi^{(2)}$ EQUATION

The two input photon energies are equal and the output photon energy is twice the input energy in order to calculate $\chi^{(2)}$ for second-harmonic generation. It was found that the contribution to $\chi^{(2)}$ from each k-state decreases sharply as k is increased from k = 0 m^{-1}, with the sum over k states for $\chi^{(2)}$ saturating by one-tenth of the Brillouin zone. Thus, the sum over k states was performed from k = 0 m^{-1} up to k corresponding to one tenth of the Brillouin zone from zone center. The sum over k-states is performed in two dimensions, *x* and *y*, corresponding to the in-plane dimensions. The spacing of k-states is determined by equation 5.

$$\Delta k = \frac{2\pi}{Na} \tag{5}$$

In equation 5, *N* is the total number of atoms along the length of the structure and *a* is the lattice constant. Using the parabolic bands approximation around zone-center along k_x and k_y, $\chi^{(2)}$ is calculated for k_x and k_y such that $\sqrt{k_x^2 + k_y^2}, \leq k_{max}$. Thus, the contribution of each state to $\chi^{(2)}$ should be radially symmetric about the origin on a k_x, k_y axis, which is observed in figure 2.

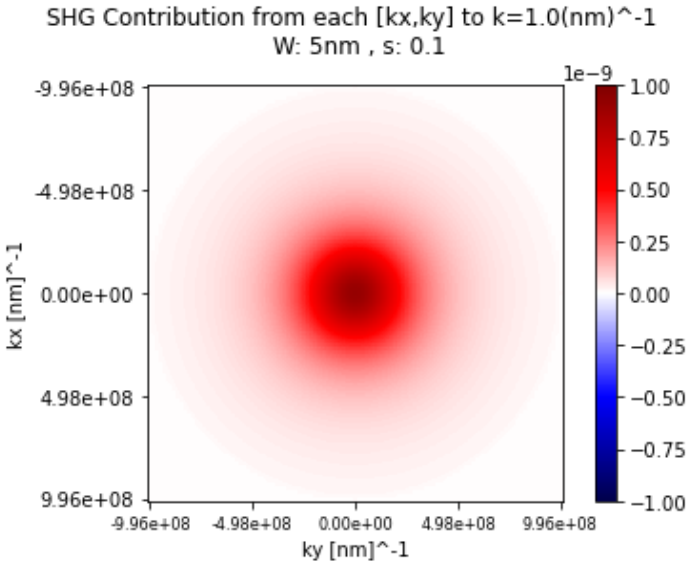

Figure 3: Contribution to $\chi^{(2)}$ from each two-dimensional k state

It is clear from figures 3a and 3b that the $\chi^{(2)}$ sum saturates by one-tenth of the Brillouin zone, which was the upper bound on the summation over k for the simulation results in this work.

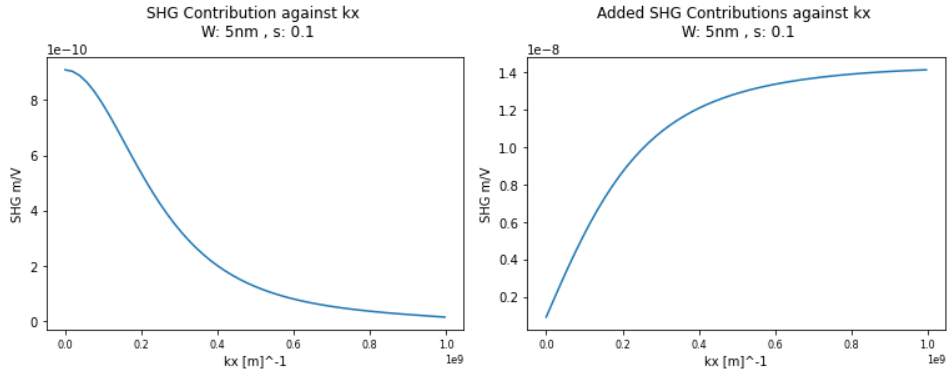

Figure 4: Saturating contribution to $\chi^{(2)}$ moving away from zone center

The calculation of $\chi^{(2)}$ from the envelope wavefunctions and energy levels was programmed using Python. The matrix elements computed using the Python code were verified using the Nextnano software's built-in matrix element calculations. The Python

program was written such that $\chi^{(2)}$ can be calculated against a sweep of any structure parameter after individual simulation files for each version of the structure are generated using Nextnano.

LINEAR COMBINATION OF ATOMIC ORBITALS

Previous theoretical calculations of $\chi^{(2)}$ used tight binding or linear combination of atomic orbitals theory to determine the wavefunctions and energy levels of the coupled quantum well structure [20]. This method is commonly used to determine the wavefunctions and bonding energies of diatomic systems, where each of the two atoms provides a potential that an electron interacts with. As the two atoms are brought closer together, the overall potential is a linear combination of the individual potentials of the atoms. As a result, two electron energy levels and their respective wavefunctions can be determined, and they are the bonding and antibonding states.

The case of coupled quantum wells can be treated the same way, where the two quantum wells are analogous to the potentials of the two atoms. It was important to determine wavefunctions and energy levels using this method to compare the $\chi^{(2)}$ calculation with published results.

The method starts by defining a "guess" wavefunction, which is a linear combination of the wavefunctions in the separate quantum wells. The ground state energy of this wavefunction can be calculated by considering the expectation value of the Hamiltonian with respect to the two wavefunctions separately, with a combination of the two wavefunctions, and by considering the overlap integral of the two separate wavefunctions. The guess wavefunction and the expectation values are defined in equations 6,7,8,9, and 10.

$$\psi_g = C_A\psi_{1A} + C_B\psi_{1B} \tag{6}$$

$$\hat{H} = -\frac{\hbar^2}{2m^*}\nabla \cdot \left(\frac{1}{m^*}\nabla\right) + V(x) \quad (7)$$

$$H_{AA} = \int_V \psi_{1A}^* \hat{H} \psi_{1B} dV \quad (8)$$

$$H_{BB} = \int_V \psi_{1A}^* \hat{H} \psi_{1B} dV \quad (9)$$

$$H_{AB} = \int_V \psi_{1A}^* \hat{H} \psi_{1B} dV \quad (10)$$

$$H_{BA} = \int_V \psi_{1B}^* \hat{H} \psi_{1A} dV \quad (11)$$

$$S_{AB} = \int_V \psi_{1A}^* \psi_{1B} dV \quad (12)$$

An important point with the Hamiltonian in equation 7 is that there is one factor of $\frac{1}{m^*}$ within the first derivative. This is necessary when considering heterostructures for which the effective mass changes with position due to material differences layer to layer. The energy of the ground state guess wavefunction is given in equation 13.

$$E_g = \frac{\int_V \psi_g^* \hat{H} \psi_g dV}{\int_V \psi_g^2 dV} \quad (13)$$

To identify the unknown coefficients in the guess wavefunction, the integrals in equation 12 are evaluated and rewritten in terms of the energy expectation values, overlap integral, and the unknown coefficients. This form is given in equation 14. This expanded form of the ground state energy is then differentiated with respect to each of the unknown coefficients, and the derivative is set equal to zero to find the local minimum. Using the two resulting equations, the ratio of the unknown coefficients is found as a function of the energy expectation values and the overlap integral. This ratio is given in equation 15.

$$E_g = \frac{H_{AA}C_A^2 + H_{BB}C_B^2 + C_A C_B H_{AB} + C_A C_B H_{BA}}{C_A^2 + C_B^2 + 2SC_A C_B} \quad (14)$$

$$\frac{C_A}{C_B} = \frac{H_{BB} - H_{AA}}{2SH_{AA} - (H_{AB} + H_{BA})} \pm \frac{\sqrt{(H_{AA} - H_{BB})^2 - (2SH_{AA} - (H_{AB} + H_{BA}))(H_{AB} + H_{BA} - 2SH_{BB})}}{2SH_{AA} - (H_{AB} + H_{BA})} \quad (15)$$

The unknown coefficients can be determined using the ration in equation 15 and normalizing the guess wavefunction. In equation 15, there are two possible outcomes corresponding to the sum and difference of the two terms. These correspond to the coefficients for the linear combination for the bonding and antibonding states.

The energy levels of the bonding and antibonding states are determined by solving for energy, E, using the matrix determinant in equation 16.

$$\begin{vmatrix} 2(E - H_{AA}) & 2SE - (H_{AB} + H_{BA}) \\ 2SE - (H_{AB} + H_{BA}) & 2(E - H_{BB-} \end{vmatrix} = 0 \qquad (16)$$

There are two solutions for the energy, E, which correspond to the bonding and antibonding states. At this point, the wavefunctions and energy levels of the two lowest lying states are determined using linear combination of atomic orbitals.

For the purpose of calculating $\chi^{(2)}$, the electron and hole wavefunctions of the two individual wells were determined using the Nextnano Schrodinger-Poisson solver. The linear combination of atomic orbitals theory was implemented in Python to determine the wavefunctions and energy levels from the individual quantum well solutions. This was then passed into the $\chi^{(2)}$ calculation program. At high levels of asymmetry, the linear combination of atomic orbitals wavefunctions and energy levels are very different from the rigorous wavefunction calculations because of the significant energy difference of the states in the thick well and thin well (which are especially thin at high asymmetry). At extreme asymmetry ($s \sim 1$), the linear combination of atomic orbitals theory predicts behavior similar to a single, thick quantum well, which is expected.

Chapter 3: Results

DIMENSIONLESS SECOND HARMONIC GENERATION COEFFICIENT

To validate the $\chi^{(2)}$ calculation, the dimensionless second harmonic generation (SHG) coefficient was calculated for GaAs/AlGaAs ACQWs with total QW widths of 5nm, 7.5nm, 10nm, and 12.5nm with QW asymmetries from $s = 0$ to $s = 0.99$. In order to compare with the results by Khurgin, the electron and hole wavefunctions and energy levels were determined using linear combination of atomic orbitals theory, and the dimensionless SHG coefficient was calculated considering only one set of transitions contributing to $\chi^{(2)}$ [20]. There was a strong peak in dimensionless SHG coefficient around 50% asymmetry and weak SHG at low asymmetry (near $s = 0$) and high asymmetry ($s = 0.99$), which agrees with Khurgin's results [20].

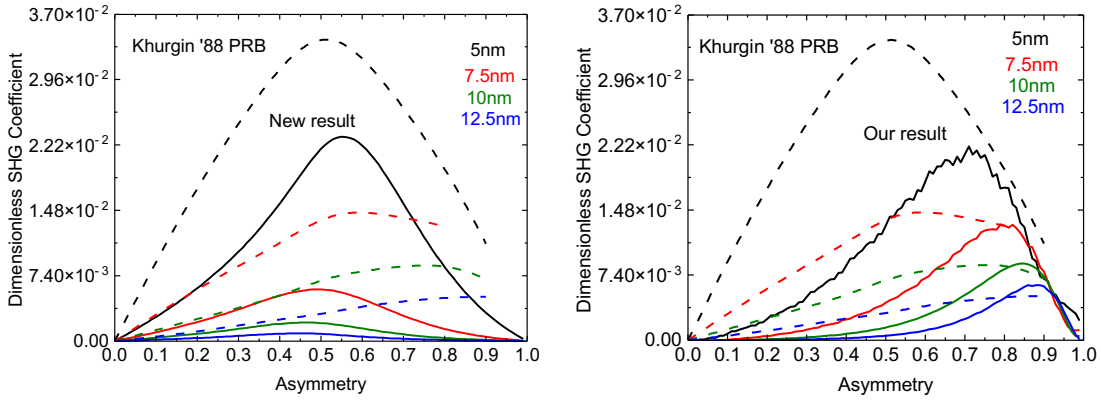

Figure 5: Dimensionless second harmonic generation coefficient

Figure 2 shows the dimensionless second harmonic generation coefficient using the calculation method presented by Khurgin, and it only account for the [m = 1, n = 1, l = 2] set of transitions in order to compare with Khurgin's results [20]. In sub-figure (a), the wavefunctions and energy levels for the individual quantum wells are determined

using Schrodinger-Poisson methods and then linear combination of atomic orbitals (LCAO) theory is used to determine the wavefunctions and energy levels for the total coupled quantum well structure. LCAO method was used to best align with Khurgin's methods, and the trends of dimensionless SHG coefficient with asymmetry and total well width match, except for a right-shifted peak with respect to asymmetry at thinner well widths. In sub-figure (b), the wavefunctions and energy levels for the coupled quantum well structures are determined using Schrodinger-Poisson methods. Although trends with total well thickness hold, it is clear that the dimensionless SHG coefficient has a peak at around s = 0.45 for all well widths, as opposed to Khurgin's result that the peak shifts to higher asymmetry with larger quantum wells.

$\chi^{(2)}$ VERSUS QUANTUM WELL ASYMMETRY

However, the total $\chi^{(2)}$ must be calculated by considering all the possible sets of transitions corresponding to the SHG process. When using rigorous wavefunction calculations, it was shown that certain sets of transitions between states (indexed by [m,n,l] in the $\chi^{(2)}$ equation) do not entirely cancel each other in the summation, so all possible transitions between the four states must be included. To show the contribution to $\chi^{(2)}$ from each set of transitions between states, $\chi^{(2)}$ [m/V] was calculated for GaAs/$Al_{0.4}Ga_{0.6}As$ ACQWs with total QW widths of 5 nm, 7.5 nm, 10 nm, and 12.5 nm for QW asymmetries ranging from s = 0 to s = 0.99. In figure 3, the $\chi^{(2)}$ contribution from each [m,n,l] set is shown with dashed lines and the total $\chi^{(2)}$ is shown with the solid line.

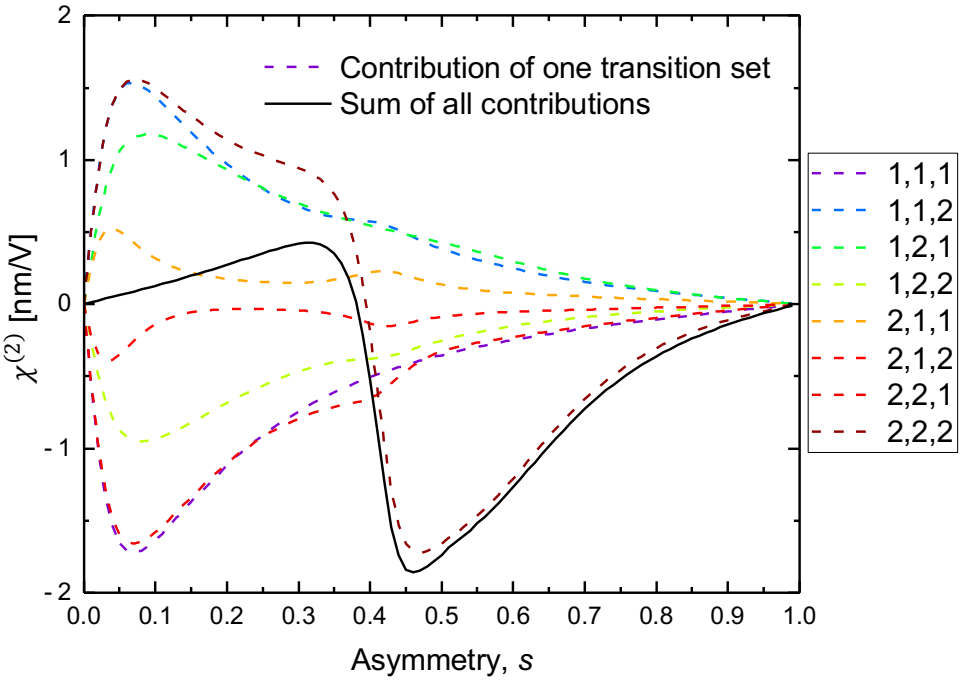

Figure 6: $\chi^{(2)}$ versus asymmetry

Figure 3 shows the calculated $\chi^{(2)}$ [nm/V] for two asymmetric coupled quantum wells with a total QW thickness of 10 nm and 1 nm barrier thickness. The asymmetry, s, of the quantum wells is swept from s = 0 to s = 0.99. The dashed lines are $\chi^{(2)}$ [nm/V] calculated for individual sets of transitions, which are indexed as [m,n,l] in accordance with equation 1. The solid line is the total $\chi^{(2)}$ [nm/V], and it is the sum of all the dashed curves. It is clear that every set of transitions shows a strong peak in $\chi^{(2)}$ [nm/V] for low asymmetries, which is associated with the heavy hole susceptibility. Each transition set also shows a weaker, second peak around s = 0.45, except for the [2,2,2] set, which changes sign at s = 0.4 and has a strong peak at s = 0.45. Because the contributions from each transition set mostly cancel with a corresponding set with $\chi^{(2)}$ [nm/V] of the opposite sign, the shape of the overall $\chi^{(2)}$ [nm/V] versus asymmetry curve follows the

[2,2,2] set beyond s = 0.4. It is important to note that $\chi^{(2)}$goes to 0 nm/V for s = 0 and s = 0.99, which is expected because both extremes of asymmetry correspond to symmetric structures.

OPTIMIZING $\chi^{(2)}$ WITH STRUCTURE PARAMETERS

The $\chi^{(2)}$ enhancement is further optimized by considering other important design parameters of the ACQW structure. The total $\chi^{(2)}$ reduces sharply as the coupling barrier thickness is increased. As this thickness is increased, the wavefunctions coupling decreases, which results in the wavefunctions of the states becoming less asymmetric and take on the symmetric shape of a wavefunction in a single QW. The overlap integrals corresponding to the matrix elements between states also decrease. The loss of QW asymmetry and the reduced matrix elements result in decreased $\chi^{(2)}$. To show the effect of coupling barrier thickness, $\chi^{(2)}$ was calculated for coupling barrier thicknesses ranging from t = 0 nm to t = 10 nm in a GaAs/$Al_{0.4}Ga_{0.6}$As ACQW with 10nm total QW thickness and asymmetry s = 0.45, and the input photon energy is off-resonant with 75 meV less than the transition energy between the hole ground state and electron ground state. This is shown in figure 4a.

The total quantum well thickness also affects $\chi^{(2)}$. As the quantum well thicknesses are increased, the first two bound state energy levels lie closer to the band edge. As a result, it is expected that structures with larger total well width have resonant $\chi^{(2)}$ at lower input photon energies. Also, as the total well width is increased, the polarization dipole can be further displaced from equilibrium. This manifests in larger intersubband matrix elements in equation 2 and larger magnitude of $\chi^{(2)}$. This effect is driven by terms where the two states in the intersubband matrix element are the same, thus representing the optical rectification, DC portion of second-order nonlinear optical

processes. In figure 2, only the [m = 1, n = 1, l = 2] case was considered, which misses these optical rectification terms, resulting in decreasing magnitude of $\chi^{(2)}$ with increasing total well width. With smaller total well widths, the states are also less confined, so the peaks of $\chi^{(2)}$ versus asymmetry are broader. The $\chi^{(2)}$ versus asymmetry calculation for GaAs/$Al_{0.4}Ga_{0.6}As$ ACQWs with 5nm, 7.5nm, 10nm, and 12.5nm total well widths is shown in figure 4b.

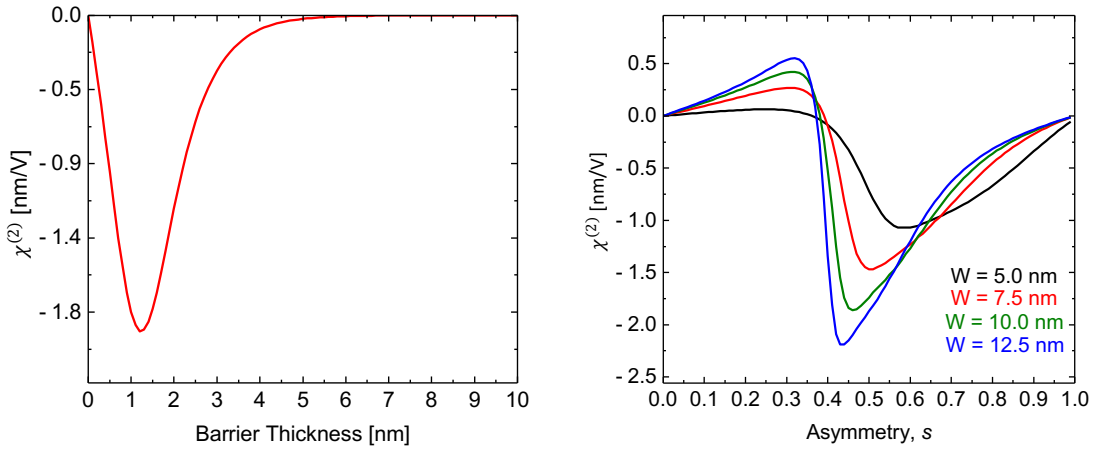

Figure 7: $\chi^{(2)}$ versus coupling barrier thickness and total quantum well thickness

Figure 4a shows the dependence of $\chi^{(2)}$ on the thickness of the barrier between coupled GaAs/$Al_{0.4}Ga_{0.6}As$ quantum wells with 10nm total well thickness and asymmetry s = 0.45. When there is no barrier, the quantum well is symmetric and thus the $\chi^{(2)}$ is 0 nm/V. As the barrier becomes large (>5 nm), the wavefunction coupling between the wells diminishes, which results in the loss of asymmetry and $\chi^{(2)}$ tends to 0 nm/V. Figure 4b shows $\chi^{(2)}$ versus asymmetry for total well widths of 5nm, 7.5nm, 10nm, and 12.5nm. Larger total well widths increase the magnitude of $\chi^{(2)}$ and have narrower peaks in $\chi^{(2)}$ with asymmetry.

TUNING $\chi^{(2)}$ RESONANT WAVELENGTH

By considering GaAs/AlGaAs ACQWs and just varying the total QW thickness, it was shown that the 50meV off-resonant wavelength for second harmonic generation can be tuned between 1.5 m and 1.7 m. These wavelengths comprise the important S, C, and L optical fiber communications bands. The $\chi^{(2)}$ is calculated for input photon wavelengths between 200 nm and 3 m in figure 5a. The $\chi^{(2)}$ versus 50 meV off-resonance wavelength and the 50 meV off-resonance wavelength against the total QW thickness are shown in figures 5b and 5c, respectively. By also considering the coupling barrier thickness, material system (for band gap and band offset control), number of ACQW periods, and other parameters, there are numerous degrees of freedom to optimize $\chi^{(2)}$ for various applications.

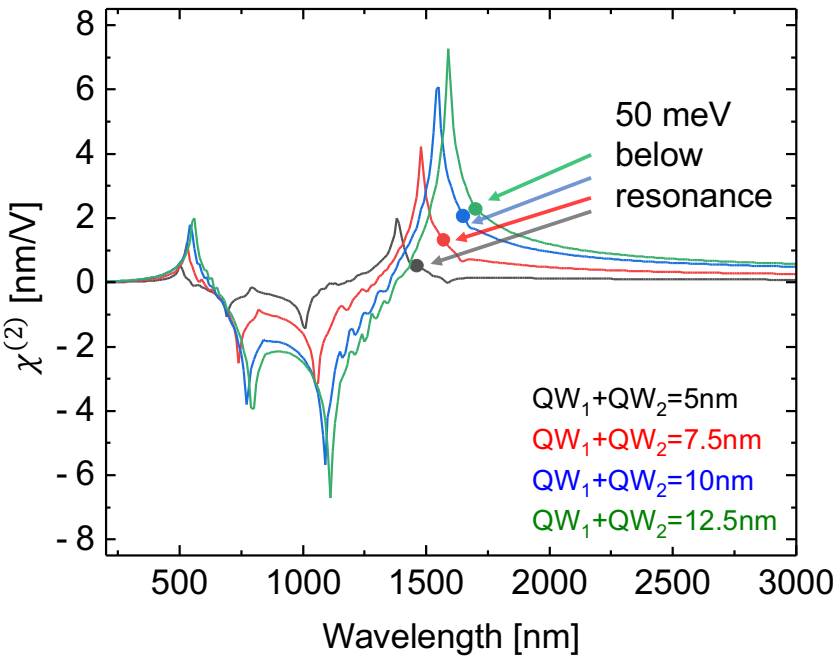

Figure 8a: $\chi^{(2)}$ versus input wavelength

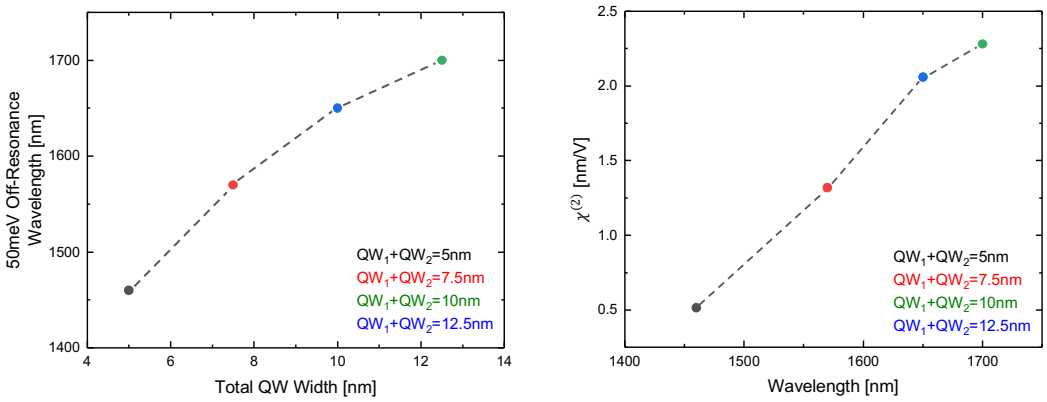

Figure 8b,c: Wavelength vs. total quantum well width, and $\chi^{(2)}$ vs. input wavelength

Figure 5 shows how $\chi^{(2)}$ depends on the input wavelength for asymmetric coupled quantum wells at asymmetry s = 0.45 with total well thicknesses of 5 nm, 7.5 nm, 10 nm, and 12.5 nm. For each structure, $\chi^{(2)}$ tends to 0 nm/V for input wavelengths less than 500 nm and greater than 3000 nm. For the short wavelengths, the photon energy is too large for second harmonic generation involving the first two electron and hole bound states in GaAs/AlGaAs quantum wells, and the long wavelength photon energy is too small for the interband SHG in this material. The peak in $\chi^{(2)}$ shifts to higher wavelengths with increasing total QW thickness because the energy levels are closer to the band edge with larger quantum wells. In sub-figure (a), the marked points correspond to 50 meV below the resonance, and this is marked because SHG experiments are typically performed slightly below resonance [20].

Changing the band offsets in the conduction and valence bands and changing the bandgap in the quantum well regions also have a significant effect on the resonant wavelength for $\chi^{(2)}$. As the band offsets increase, electrons and holes are more confined in the quantum wells and the bound state energies become more spaced out and shift further away from the band edge. As a result, it is expected that the resonance for $\chi^{(2)}$

will shift to lower wavelengths. Since the ground state to ground state interband transition is very close to the bandgap energy, changing the bandgap of the quantum well regions will significantly affect the resonant $\chi^{(2)}$ wavelength. As the bandgap is decreased, the resonance will shift to longer wavelengths.

An important future study will be to understand how the bandgap affects the strength of interband $\chi^{(2)}$. As the bandgap energy is decreased, the interband transition between the heavy hole ground state and the electron ground state will be closer in energy to intersubband transitions in the conduction and valence bands. This should significantly increase the strength of $\chi^{(2)}$ specifically for the case of second harmonic generation. It would also be fruitful to calculate the $\chi^{(2)}$ for sum frequency and difference frequency generation processes. Especially for a system such as GaAs/AlGaAs, for which the bandgap energy is significantly larger than the intersubband transition energies available, one would expect strong $\chi^{(2)}$ for sum-/difference- frequency generation processes where one input photon has energy close to the bandgap and the second photon has energy close to an intersubband transition energy.

Chapter 4: Experimental Approach

COUPLED QUANTUM WELL GROWTH

The purpose of using the GaAs/AlGaAs material system for the asymmetric coupled quantum well simulations was to be able to easily transition to experiment. The GaAs/AlGaAs system has very well known linear optical properties, and the growth of $Al_xGa_{1-x}As$ for a wide range aluminum concentrations is readily achievable using molecular beam epitaxy (MBE). Furthermore, the sample can be grown on a GaAs substrate to enable lattice matching and good material quality. Throughout the simulation work, the structure parameters were chosen to be compatible for MBE growth. Layer thicknesses can precisely be grown to within a tenth of a nanometer, allowing for QW thicknesses that require angstrom precision to reach a target value of asymmetry. Also, the total structure thickness, including buffer layers, for a single asymmetric coupled quantum well with 10nm total well thickness is 41nm. This is thin enough for short overall growth times, allowing to grow multiple samples in a single day.

For the samples, asymmetric coupled quantum wells were grown with various asymmetries with a 10 μm total QW thickness, 1 nm coupling barrier thickness, and 60% aluminum composition in the AlGaAs barrier layers. The asymmetries that were grown were s = 0, 0.1, 0.35, 0.42, and 0.60. At the time (summer 2022), simulation results were showing two strong peaks in $\chi^{(2)}$ around s = 0.1 and 0.42. The symmetric case, s = 0 was grown as a control, and it was expected that the second harmonic signal would be weak. The second harmonic response for the symmetric case would not be 0 m/V because GaAs and AlGaAs are non-centrosymmetric and have nonzero bulk $\chi^{(2)}$. For the s = 0.1 case, two samples were grown. The first sample had the thinner well closer to the surface and the second sample switched the order of the quantum wells such that the thinner quantum

well is closer to the substrate. Simulation results showed that switching the order of the quantum wells changes the sign of the overall $\chi^{(2)}$, which corresponds to polarization in the opposite direction. For all other asymmetries, only one sample was grown with the thinner quantum well closer to the surface. The sample at s = 0.35 was grown because simulation results suggested a local minimum in the $\chi^{(2)}$ versus asymmetry between the peaks at s = 0.1 and s = 0.45. The sample at s = 0.60 was grown to show that the strength of the second harmonic response should diminish beyond the second peak at s = 0.45. The data presented in the results section of this thesis do not show this double peak. This is because at the time, only [m,n,l] terms corresponding to second harmonic generation were being considered in the summation. However, the complete calculation of $\chi^{(2)}$ requires that all terms, including optical rectification terms, be considered in the sum.

Additional control samples were a bare GaAs wafer, 41 nm of GaAs grown on the GaAs substrate, and 41 nm of $Al_{0.6}Ga_{0.4}As$ grown on GaAs. These controls were included to measure the bulk second harmonic response of the constituent materials of the asymmetric coupled quantum well structures. It was expected that the asymmetric structure would enhance the second harmonic response compared to these controls.

When growing the samples using MBE, the GaAs growth rate was 0.409 Å/s. The gallium flux was calculated to be 9.07 x 10^{-3} atoms/Å^{2}s, and the aluminum flux for 60% aluminum composition was 13.6 x 10^{-3} atoms/Å^{2}s. On the first growth day, the s = 0, 0.1, 0.1 inverted, and 0.35 samples were grown. During the growth of the symmetric, s = 0, sample, the arsenic cell cooled while growing the cap layer. Thus, the s = 0 sample was regrown on the second day. The second day saw the growths of the s = 0, 0.42, 0.60 samples and the AlGaAs on GaAs control.

SECOND HARMONIC GENERATION MEASUREMENT EXPERIMENT

The experiment to measure the second harmonic generation uses laser light incident on the sample at an angle to generate a second harmonic signal in reflection. Starting from the laser, the light passes through a half wave plate to set the polarization of the incident light. A mirror is used to direct the light toward a lens, which focuses the polarized laser light on the surface of the sample. The lens is positioned such that the light is incident on the surface at a 45 degree angle. The optics up to this point are considered the "input side" of the setup. Another lens is positioned to collect the output light. This lens is also positioned at 45 degrees to the surface of the sample. A mirror is used to direct the output light to a polarizer to restrict whether the output is p- or s-polarized. A filter is used to selectively pass light only at the second-harmonic wavelength. Finally, a photomultiplier tube and photon counter are used to measure the second harmonic response in units of counts per second [16].

All the optics on the input side of the setup are chosen for optimal performance at the input wavelength. The optics on the output side are chosen based on the second-harmonic wavelength. The photomultiplier tube is also chosen for operation at the intended second harmonic wavelength. Additionally, the setup is covered on all sides and the lab lights are turned off to minimize background photon detection and the resulting noise.

Initial runs of the experiment were performed with input wavelengths of 780 nm and 1550 nm. When using the 780 nm input, the input laser power was 80 mW, resulting second harmonic response on the order of 1 million counts/second. The 1550nm wavelength was only at ~1 mW, and the resulting detection was on the order of 10,000 counts/second. In both cases, the data did not show a significant difference in second harmonic response between the controls and the asymmetric coupled quantum well

samples. However, the signal was significantly weaker when using s-polarized input light compared to p-polarization. This is expected because in the case of s-polarization, the electric field component of the EM radiation is parallel to the plane of the quantum wells. When using p-polarized input, a component of the electric field is perpendicular to the plane of the quantum wells, which induces second harmonic generation. This data indicates that the second harmonic response is dominated by the bulk $\chi^{(2)}$ response of the GaAs and AlGaAs layers and primarily the GaAs substrate.

To reduce the second harmonic response from the substrate, the samples need to be prepared differently. The substrate should be a material with no $\chi^{(2)}$, especially at the target wavelengths in the near-IR. However, it is not possible to grow GaAs/AlGaAs structures directly on such a substrate, so the approach will be to grow the structure on a GaAs substrate using an AlAs etch release layer. By etching away the AlAs, it will be possible to transfer the coupled quantum well structure to a substrate such as quartz. This is the next goal on the experimental side of the project.

CHAPTER 5: CONCLUSIONS

This work shows that semiconductor coupled multi-quantum well structures can be designed for strong second-order optical nonlinearity at wavelengths tailored for particular applications. While this work focused on the GaAs/AlGaAs system, there is potential to utilize semiconductor alloys with larger conduction band offsets or to better lattice match with a given substrate. The multi-quantum well approach is well implemented using digital alloy growth techniques, and extending the structure to many periods of coupled quantum wells leads to superlattices with strong, tailorable nonlinearities.

Semiconductor coupled quantum well structures with enhanced nonlinearity can be used in conjunction with metasurfaces for field concentration or to change the polarization or direction of the input and output light. Waveguides made from these structures could also enable smaller electro-optic modulators by reducing the necessary interaction length.

There were several main aspects of this project discussed in this thesis. The first step was to develop a simulation platform for determining the wavefunctions and energy levels of the electron and heavy hole states of a coupled quantum well structure. The results of these quantum mechanical calculations were used to calculate $\chi^{(2)}$ using the density matrix formalism. After refining the simulations, the methods were verified by comparing to literature studies of $\chi^{(2)}$ versus quantum well asymmetry in GaAs/AlGaAs asymmetric coupled quantum wells. Then, the effects of various structure parameters on $\chi^{(2)}$ were understood through simulations. An important result was identifying that the GaAs/AlGaAs asymmetric coupled quantum well structure can enhance the $\chi^{(2)}$ for near-IR wavelengths, which are important for optical communications applications. Then, a set

of GaAs/AlGaAs asymmetric coupled quantum well structures were grown using MBE. Although second harmonic generation measurements have not been fruitful yet due to the bulk second harmonic response of the GaAs substrate, a new sample growth and preparation method has been identified.

The next steps on the simulation side of the project are to explore new semiconductor material systems for further enhanced nonlinearities at wavelengths of interest. Also, the digital alloy structure will be explored as a platform for enhanced nonlinearities. On the experimental side, a new set of coupled quantum well samples will be grown and transferred to a non-$\chi^{(2)}$ substrate in order to perform SHG measurements without the overpowering signal from the bulk.

References

[1] P. A. Franken, A. E. Hill, C. W. Peters, and G. Weinreich, "Generation of Optical Harmonics," *Phys. Rev. Lett.*, vol. 7, no. 4, pp. 118–119, Aug. 1961, doi: 10.1103/PhysRevLett.7.118.

[2] C. Wang *et al.*, "Ultrahigh-efficiency wavelength conversion in nanophotonic periodically poled lithium niobate waveguides," *Optica*, vol. 5, no. 11, p. 1438, Nov. 2018, doi: 10.1364/OPTICA.5.001438.

[3] J. S. Pelc *et al.*, "Long-wavelength-pumped upconversion single-photon detector at 1550 nm: performance and noise analysis," *Opt. Express*, vol. 19, no. 22, p. 21445, Oct. 2011, doi: 10.1364/OE.19.021445.

[4] C. Langrock, S. Kumar, J. E. McGeehan, A. E. Willner, and M. M. Fejer, "All-optical signal processing using /spl chi//sup (2)/ nonlinearities in guided-wave devices," *J. Lightwave Technol.*, vol. 24, no. 7, pp. 2579–2592, Jul. 2006, doi: 10.1109/JLT.2006.874605.

[5] M. Stefszky, V. Ulvila, Z. Abdallah, C. Silberhorn, and M. Vainio, "Towards optical-frequency-comb generation in continuous-wave-pumped titanium-indiffused lithium-niobate waveguide resonators," *Phys. Rev. A*, vol. 98, no. 5, p. 053850, Nov. 2018, doi: 10.1103/PhysRevA.98.053850.

[6] M. Jankowski *et al.*, "Ultrabroadband nonlinear optics in nanophotonic periodically poled lithium niobate waveguides," *Optica*, vol. 7, no. 1, p. 40, Jan. 2020, doi: 10.1364/OPTICA.7.000040.

[7] R. W. Boyd, *Nonlinear optics*. 2020.

[8] G. Sinatkas, T. Christopoulos, O. Tsilipakos, and E. E. Kriezis, "Electro-optic modulation in integrated photonics," *Journal of Applied Physics*, vol. 130, no. 1, p. 010901, Jul. 2021, doi: 10.1063/5.0048712.

[9] C. Kachris and I. Tomkos, "A Survey on Optical Interconnects for Data Centers," *IEEE Commun. Surv. Tutorials*, vol. 14, no. 4, pp. 1021–1036, 2012, doi: 10.1109/SURV.2011.122111.00069.

[10] K. Powell *et al.*, "Integrated silicon carbide electro-optic modulator," *Nat Commun*, vol. 13, no. 1, p. 1851, Dec. 2022, doi: 10.1038/s41467-022-29448-5.

[11] X. Chen, D. Taguchi, T. Manaka, M. Iwamoto, and Z. L. Wang, "Direct probing of contact electrification by using optical second harmonic generation technique," *Sci Rep*, vol. 5, no. 1, p. 13019, Oct. 2015, doi: 10.1038/srep13019.

[12] E. W. Gaul *et al.*, "Design of the Texas petawatt laser," in *2005 Quantum Electronics and Laser Science Conference*, Baltimore, MD, USA: IEEE, 2005, pp. 26–28. doi: 10.1109/QELS.2005.1549364.

[13] Y. R. Shen, *The principles of nonlinear optics*, Wiley classics library ed. in Wiley classics library. Hoboken, N.J: Wiley-Interscience, 2003.

[14] C. Wang *et al.*, "Integrated lithium niobate electro-optic modulators operating at CMOS-compatible voltages," *Nature*, vol. 562, no. 7725, pp. 101–104, Oct. 2018, doi: 10.1038/s41586-018-0551-y.

[15] J. Lu, A. Al Sayem, Z. Gong, J. B. Surya, C.-L. Zou, and H. X. Tang, "Ultralow-threshold thin-film lithium niobate optical parametric oscillator," *Optica*, vol. 8, no. 4, p. 539, Apr. 2021, doi: 10.1364/OPTICA.418984.
[16] N. D. Foster, A. K. Rockwell, J. A. McArthur, B. S. Mendoza, S. R. Bank, and M. C. Downer, "A Study of Second-Order Susceptibility in Digital Alloy-Grown InAs/AlSb Multiple Quantum Wells," *Advanced Optical Materials*, vol. 10, no. 15, p. 2102845, Aug. 2022, doi: 10.1002/adom.202102845.
[17] M. M. Fejer, S. J. B. Yoo, R. L. Byer, A. Harwit, and J. S. HarrisJr., "Observation of extremely large quadratic susceptibility at 9.6 – 10.8 μ m in electric-field-biased AlGaAs quantum wells," *Phys. Rev. Lett.*, vol. 62, no. 9, pp. 1041–1044, Feb. 1989, doi: 10.1103/PhysRevLett.62.1041.
[18] N. Bloembergen, *Nonlinear optics*, 4. ed., Repr. Hackensack, N.J.: World Scientific, 2010.
[19] J. Khurgin, "Second-order susceptibility of asymmetric coupled quantum well structures," *Appl. Phys. Lett.*, vol. 51, no. 25, pp. 2100–2102, Dec. 1987, doi: 10.1063/1.98960.
[20] J. Khurgin, "Second-order nonlinear effects in asymmetric quantum-well structures," *Phys. Rev. B*, vol. 38, no. 6, pp. 4056–4066, Aug. 1988, doi: 10.1103/PhysRevB.38.4056.
[21] M. M. Choy and R. L. Byer, "Accurate second-order susceptibility measurements of visible and infrared nonlinear crystals," *Phys. Rev. B*, vol. 14, no. 4, pp. 1693–1706, Aug. 1976, doi: 10.1103/PhysRevB.14.1693.
[22] S. Birner *et al.*, "nextnano: General Purpose 3-D Simulations," *IEEE Trans. Electron Devices*, vol. 54, no. 9, pp. 2137–2142, Sep. 2007, doi: 10.1109/TED.2007.902871.